RSC Advances

ROYAL SOCIETY OF CHEMISTRY

www.rsc.org/advances

Sol-gel synthesis of nanocrystals-constructed hierarchically porous TiO_2 based composites for lithium ion batteries

Wenjun Zhu,[a] Hui Yang,[a] Kazuki Nakanishi,[b] Kazuyoshi Kanamori,[b] Xingzhong Guo*[a]

Hierarchically porous TiO_2 based composites (pure TiO_2 and TiO_2/Carbon (TiO_2/C) composite) were synthesized by a facile sol-gel process followed by post-calcination. Poly(vinylpyrrolidone) (PVP) acts as a phase separation inducer as well as a carbon source. The as-prepared TiO_2 based composites possess an interesting hierarchically porous structure constructed by cocontinuous macropores and mesoporous skeletons consisting of interconnected nanocrystals and *in situ* distributed carbon. The hierarchically porous TiO_2/C composite shows excellent electrochemical performances with fast lithium ion diffusion and electronic transport, resulting from hierarchically porous structure and conductive carbon material. The TiO_2/C composite calcined at 500 °C exhibits the highest BET surface area of 170 m^2 g^{-1}, superior cycling stability (delivers a remarkable discharge capacity of 132 mAh g^{-1} at 1 C after 100 cycles) and excellent rate capability (over 96 mAh g^{-1} at 30 C rate). The results indicate that these hierarchically porous TiO_2 based composites could be promising anode materials for high performance lithium ion batteries.

[a]*School of Materials Science and Engineering, Zhejiang University, 38 Zheda Road, Xihu District, Hangzhou 310027, China. E-mail: msewj01@zju.edu.cn (X.Z. Guo)*

[b]*Department of Chemistry, Graduate School of Science, Kyoto University, Kitashirakawa, Sakyo-ku, Kyoto 606-8502, Japan.*

Introduction

Titanium oxide (TiO_2) has received considerable attention because of its photoelectric properties, biocompatibility and chemical stability, and has been extensively applied in various kinds of fields such as photocatalysis,[1,2] sensing[3], dye-sensitized solar cells,[4-6] and lithium-ion batteries (LIBs),[7-11] etc. Especially, in the case of LIBs applications, TiO_2 is regarded as one of the most promising anode material due to its long cycle life, low cost, environmental compatibility, and low volume expansion.[7,12,13] Furthermore, compared with the traditional graphite anode materials, TiO_2 anode shows a relatively higher lithium insertion/extraction voltage (higher than 1.5 V *vs* Li^+/Li) to ensure adequate safety by efficiently avoiding the formation of solid electrolyte interphase (SEI) films and lithium dendrites.[14,15] However, the practical application of the TiO_2 anode is still hampered by limited rate capability arising from its low intrinsic electrical conductivity (10^{-12} S cm^{-1}).[16,17]

Recently, great efforts have been devoted to circumvent the drawback of poor rate capability of TiO_2 electrodes.[18-23] Fabrication of porous structure is an effective approach to improve the electrochemical performance by supporting sufficiently rapid transport of both lithium ions and electrons.[20,24-29] Different types of pores have various effects on the electrochemical of electrodes.[24,30,31] The micropores provide more active sites for Li-insertion by increasing specific surface area, while the mesopores reduce the length of lithium ions and electrons by providing interconnected nanopaths. Meanwhile, the macropores could effectively accommodate

electrolytes for the electrochemical reaction. Thus, hierarchically porous structure could offer a good choice to improve electrode properties with multiple benefits arising from different pore size regimes. Additionally, another effective strategy to improve electron transport by decorating TiO_2 materials with high conductivity materials, such as metals,[32] metal oxides,[33,34] and carbonaceous materials.[16,24,26,35-42] Among these conductivity materials, carbonaceous materials have been demonstrated to effectively increase electron transport to further enhance the electrochemical performance of TiO_2 electrode, especially the rate capability. As a result, it is highly desirable to design and fabricate new TiO_2 electrode materials combining hierarchically porous structure with highly conductive carbonaceous materials.

In this paper, we report a facile and convenient method for preparing hierarchically porous pure TiO_2 and TiO_2/C composite by a combination of sol-gel with the aid of PVP, followed by post-calcination in air and argon atmosphere, respectively. The specific procedure is schematically illustrated in Fig. 1. The as-prepared TiO_2 based composites reveal some distinguishing features: (i) Both of the pure TiO_2 and TiO_2/C composite show a hierarchically porous structure (Fig. 1b) with a high specific surface area, enlarging the contact surface between electrode and electrolyte. (ii) The cocontiuous skeletons are constructed by many interconnected nanocrystals with sizes of 10-30 nm (Fig. 1c), which shorten the diffusion distance of Li-ion for the fast charge-discharge cycles. (iii) During the procedure, PVP is used as a phase separation inducer as well as a carbon source resulting in the *in situ* formed TiO_2/C composites, which ensures an intimate contact of carbon and TiO_2, providing

excellent electrical conductivity for high rate performance. The structure and electrochemical performance of pure TiO_2 and TiO_2/C composite calcined at different temperatures are investigated. The resultant TiO_2/C composite exhibits excellent rate and cycling performance due to the synergistic effect of the hierarchically porous structure resulting in large specific surface area and enhanced electrical conductivity ascribe to the *in situ* formed carbon derived from PVP.

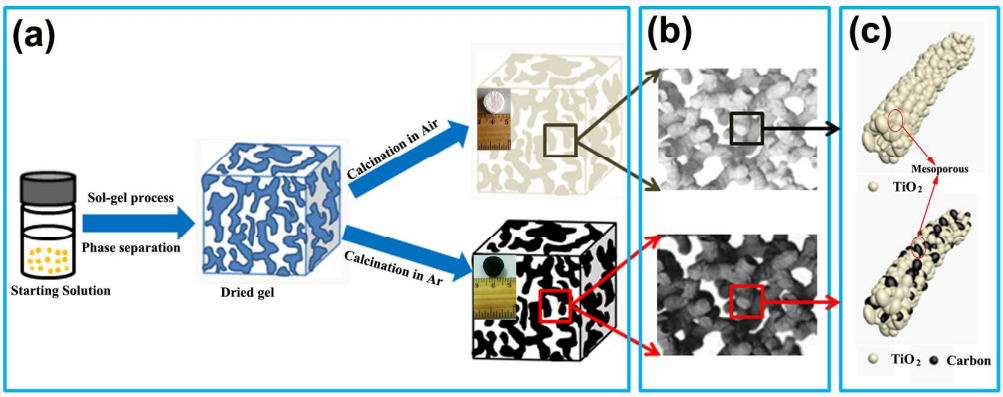

Fig. 1 (a) Schematic illustration of the experimental procedure of hierarchically porous TiO_2-based monoliths. (b) Macrochannels are derived from phase separation. (c) Mesoporous skeletons are composed of interconnected nanocrystals and *in situ* distributed carbon.

Experimental

Materials synthesis

$TiOSO_4$•xH_2O (Sigma-Aldrich) was utilized as the titanium source. Mixtures of distilled water and ethylene glycol (EG, Sinopharm Chemical Reagent Co., Ltd (China)) were used as the solvents. Formamide (FA, Shanghai Lingfeng Chemical Reagent Co., Ltd) was utilized to initiate the gelation. Poly(vinylpyrrolidone) (PVP, Sigma-Aldrich, M_w=10,000) was used as a polymer to induce the phase separation and a carbon source after calcination in an argon atmosphere. All chemicals were of analytical grade and used as received without further

purification.

The experimental procedure of TiO_2-based composites is shown in Fig. 1a. The typical synthesis of the titanium sol was as follows in detail. Firstly, 1 g $TiOSO_4$•xH_2O was dissolved in distilled water and continuously stirred for 2 h to obtain a clear homogeneous solution. Then 0.6 mL of ethylene glycol (EG) and 0.2 g of Poly(vinylpyrrolidone) (PVP) were added into the above solution, and after stirring for 30 min to obtain pale yellow solution, 0.5 mL of Formamide (FA) was added under vigorous stirring. The mix solution was kept in a sealed container at 60 ^{o}C for gelation. The whole gelation process can be finished within about 2 h, during the process the colour of solution was changed from pale yellow to clear and finally to white, and the milk white monolith can be obatined after the gelation. The wet gel was subsequently aged at 60 ^{o}C for 12 h, then subjected to solvent exchange to remove the residues by ethanol for 3 times every 12 h and 2-propanol for 12 h, respectivley. The dry gel was obtained after evaporation-dried at 40 ^{o}C for a week, which presents a about 3%-5% volume shrinkage induced by the solvent exchange and subsequent evaporation drying. Some of the dried gels were heat-treated at various temperatures (500, 600 and 800 ^{o}C) for 4 h in air to obtain pure TiO_2, respectively, and TiO_2/C composites were prepared by calcination of the dried gel in an argon atmosphere.

Structure characterizations

The crystallinity of the samples was characterized using powder X-ray diffractometry (XRD; X'Pert Pro diffractometer with a Cu Kα radiation, λ

=0.15418 nm). The morphology of the samples was observed using scanning electron microscopy (SEM; Hitachi S-4800) and transmission electron microscopy (TEM; FEI, Tecnai G2 F20), equipped with an energy dispersive spectroscopy (EDS) detector. Fourier transform infrared spectra (FTIR) of powder samples diluted with KBr were recorded with a Bruker VERTEX 70. The composition of the products was performed using X-ray photoelectron spectroscopy (XPS, Escalab 250Xi, UK), equipped with a hemispherical electron energy analyzer using a monochromatic Al Kα X-ray radiation (15 KV, 1486.6 eV) under a vacuum pressure of 5×10^{-10} Torr. A wide-scan survey spectrum was performed on each sample to determine the elements state at the surface. High-resolution spectra of the Ti 2p and O 1s core lines were collected using a pass energy of 20 eV, a step size of 0.05 eV, and a sweep time of 180 s. The thermal decomposition behavior of the dried gel and the carbon content of TiO_2/C composite were examined by thermogravimetric analysis (TGA, TA Q500) at a heating rate of 10 °C min^{-1} from room temperture (25 °C) to 800 °C in air and N_2 atmosphere, respectively. Measurements of Raman spectra were performed on a Renishaw InVia Raman Spectrometer under a backscattering geometry (λ=532 nm). Nitrogen adsorption-desorption apparatus (AUTOSORB-1-C) was used to characterize the meso- and micropores of the samples. The pore size distribution was calculated using the Barrett–Joyner–Halenda (BJH) method based on the adsorption branch.

Electrochemical measurements

Electrochemical experiments were carried out using standard CR 2025 type coin half

cells. The as-prepared samples (pure TiO_2 and TiO_2/C composite) were mixed with carbon black (Super P) and polyvinylidene fluoride (PVDF) binder at a weight ratio of 80:10:10 in N-methyl-2-pyrrolidene (NMP) solution. The slurry was pasted on a Cu foil and dried in a vacuum oven at 120 ^{o}C for 12 h to serve as the working electrode. The weight of the active material in the electrode sheet was about 2.5 mg cm^2. The pure lithium foil was used as both counter electrode and reference electrode. A solution of 1M $LiPF_6$ in ethylene carbonate (EC)/dimethyl carbonate (DMC) (1:1 by volume) was used as the electrolyte with a polypropylene microporous film (Cellgard 2300) as the separator. Galvanostatical charge–discharge experiments were tested at different current densities in a voltage range of 1.0–3.0 V on a battery test system (Shenzhen Neware Battery, China). Cyclic voltammetry (CV) measurements and Electrochemical impedance spectroscopy (EIS) tests were carried out on a CHI660b electrochemical workstation (Shanghai Chenhua, China). The CVs were obtained over the potential range of 1.0–3.0 V at a scanning rate of 0.1 mV s^{-1} and the impedance spectra measurements were tested with the frequency ranging from 0.1 Hz to 100 KHz by applying a sine wave with amplitude of 5.0 mV.

Results and discussion

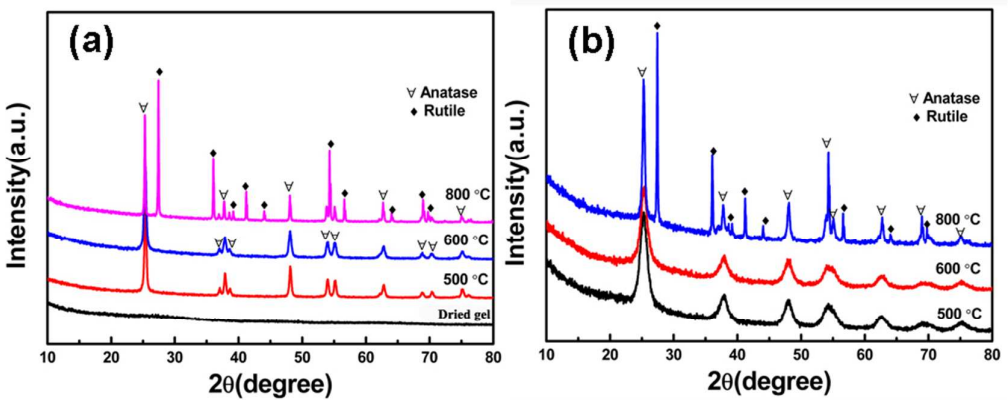

Fig. 2 XRD patterns of (a) pure TiO_2 and (b) TiO_2/C composite calcined at different temperatures.

Fig. 2 shows X-ray diffraction (XRD) patterns of the as-prepared pure TiO_2 and TiO_2/C composite. It can be seen that after calcined at 500 and 600 °C, all the diffraction peaks of both samples can be indexed to anatase TiO_2 with a tetragonal structure (JCPDS 65-5714) without the formation of a new phase, indicating that the amorphous titanium was converted to crystalline TiO_2 completely.[24] It can be seen that the peaks appear in TiO_2/C composite samples (Fig. 2b) are broader than those of pure TiO_2 samples (Fig. 2a). It indicates that TiO_2/C composite possesses relatively smaller crystal size, which is possibly owing to the interference of the carbon compositon in TiO_2/C composite. The crystal of rutile (JCPDS 21-1276) marked by black diamond appears when the annealing temperature is raised to 800 °C.

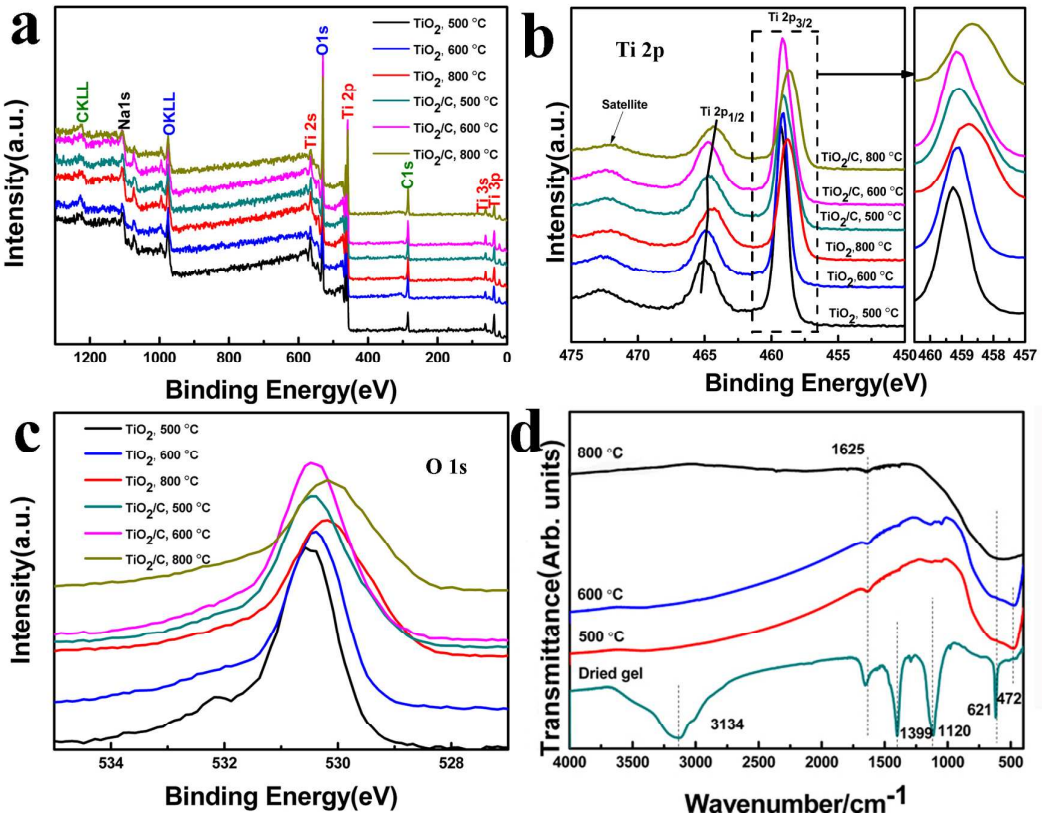

Fig. 3 XPS spectrum of pure TiO_2 and TiO_2/C composite calcined at different temperatures: (a) full survey scan spectrum, (b) Ti 2p (left) and an enlarged figure (right) of Ti $2p_{3/2}$ state in valence band marked by the dashed rectangle rectangle in left and (c) O1s peak. (d) FT-IR spectra of the dried gel and pure TiO_2 samples calcined at different temperatures.

X-ray photoelectron spectroscopy measurements were performed to confirm the oxidation states of Ti in pure TiO_2 and TiO_2/C composite. All the binding energies (BE) were measured in reference to the C1s peak at 284.80 eV. Pure TiO_2 and TiO_2/C composite display the similar survey spectrum, as shown in Fig. 3a. The signals originating from Ti 2p, O 1s and C 1s are easily detected, indicating the existence of Ti, O, and C. The specific information of binding energies of Ti and O are tabulated in Table S1. Fig. 3b displays the XPS spectrum of Ti 2p doublet peaks; the binding energies of Ti $2p_{1/2}$ and Ti $2p_{3/2}$ were observed at approximately 464 eV and 459 eV, respectively, which are characteristic peaks of Ti^{4+}.[43] Additionally, it can be seen that the peak of Ti $2p_{1/2}$ and Ti $2p_{3/2}$ shifts

toward lower binding energy with increasing calcination temperature, which may be contributed to trace amount of Ti^{3+}.[44] However, none of the characteristic peaks of Ti^{3+} (457.2 eV, BE) and/or Ti^{2+}(455.3 eV, BE) can be observed from the Ti 2p spectrum.[45] It indicates that the main composition phase of the as-prepared products is TiO_2. The result can be further confirmed by the O1s spectrum (Fig. 3c) with a main strong binding energy peak at about 530 eV (as shown in Table S1), characteristic of the Ti-O-Ti bonds in TiO_2. The weak peak at 532.18 eV (TiO_2 sample, 500 °C) can be atrributed to surface -OH or adsorbed water.[16,36,46]

The FTIR spectra of the dried gel and pure TiO_2 samples collected in the range of 400-4000 cm^{-1} is shown in Fig. 3d. The broad absorption band at 3134 cm^{-1} is assigned to the stretching vibration mode of N-H resulting from FA.[47,48] The peak at 1625 cm^{-1} corresponds to the plane bending vibration of O-H bending vibrations of water which adsorbed physically on the surface of the TiO_2 samples due to the strong hydrophilic quality of the TiO_2.[49] The peak at 1120 cm^{-1} is due to the C-O stretching vibrations, and the peak at 1399 cm^{-1} is assigned to the C-H stretching vibration derived from PVP (Fig.S1a), indicating that PVP is preferentially distributed to the gel solid phase[50,51] and these peaks disappeared after calcination above 500 °C.[28,36] The peak locates at 621 cm^{-1} is characteristic bending vibrations of Ti-OH bonds, which shifts to a low peak at 472 cm^{-1} after calcination, corresponding to the bending vibration of Ti-O bond.[52] These FT-IR spectra results indicate that the amorphous titanium gel completely transforms to TiO_2 after calcination above 500 °C. Moreover, similar FT-IR spectra curves (Fig. S1b) can

be observed from TiO_2/C composites calcined at different temperatures. During the reaction process, ethylene glycol works as a chelating agent which coordinates with titanium ion through hydrogen bonding to attain the better control of the gelation. FA is a highly polar solvent with hydrogen bonding and is hydrolyzed to produce ammonia and formic acid in the presence SO_4^{2-} (hydrolysis of $TiOSO_4 \cdot xH_2O$), increasing the pH of solution gradually, which accelerates the polycondensation reaction to adjust the gelation time. Surfactant of PVP was applied as an phase separation inducer, which leads to phase separation into the solvent-rich and gel-rich phases due to spinodal decomposition, resulting in well-defined macroporous gels (as discussed below) after gelation and drying[53-55].

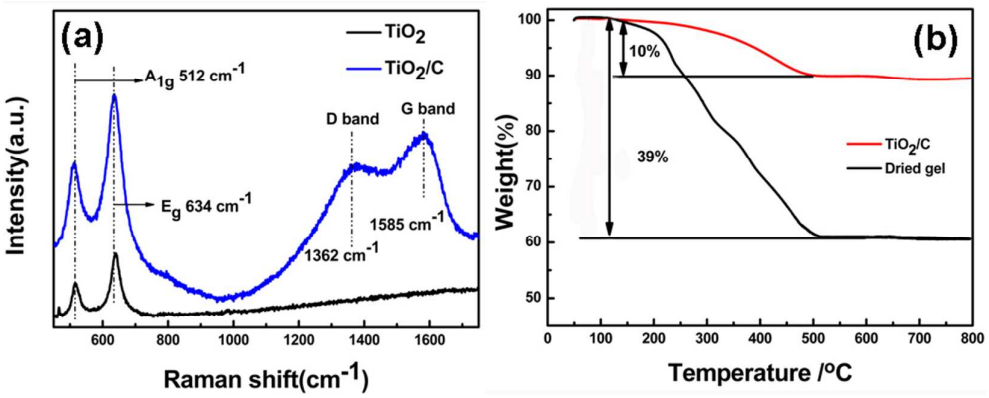

Fig. 4 (a) Raman spectra of pure TiO_2 and TiO_2/C composite. (b) TGA curves of dried gel and TiO_2/C composite in air, all the samples obtained calcined at 500 °C.

Fig. 4a reveals the Raman spectra of pure TiO_2 and TiO_2/C composite. Two strong vibrational bands at 512 and 634 cm^{-1} are observed in the spectra of both samples, which belong to A_{1g} and E_g vibration mode of anatase TiO_2, respectively.[56] Moreover, two broad peaks located at 1362 and 1585 cm^{-1} are detected in the spectra of TiO_2/C composite, corresponding to the A_{1g} vibration mode of the

disordered carbon (D bond) and the E_{2g} vibration mode of the ordered graphitic carbon (G bond), respectively.[57] The Raman spectra results comfirm that PVP was converted to carbon after calcination in an argon atmosphere. Additionally, the ID/IG value (ratio of the intensity of D Raman peak and G Raman peak) of the TiO_2/C composite is 0.84, which is favorable to provide good electrical conductivity and maintain the structural integrity of TiO_2/C composite during repeated charge/discharge cycling.

Thermal analysis was performed to evaluate the thermal decomposition behavior of dried gel and the actual carbon content of TiO_2/C composite. Fig. 4b exhibits the thermal decomposition characteristic curve of dried gel and TiO_2/C composite. For dried gel, there is a distinct weight loss of about 39% occurred from 120 to 500 ^oC, and the weight keeps stable later. The big weight loss can be attributed to the elimination of absorbed/trapped water, chemical reaction of dried gel converts to TiO_2 and the decomposition of PVP. The TGA curve of dried gel in N_2 atmosphere (Fig. S2) shows the similar thermal behavior with a weight loss of about 28% during the calcination process. The difference value of weight after calcined in different atmosphere (air and N_2) is calculated to about 11%, which is ascribed to the carbon resulting from the pyrolysis of PVP. Furthermore, under the same heat treatment process, a 10 % weight loss is observed for the TiO_2/C composite, which is mainly ascribed to the combustion of carbon to CO_2. That is to say, the carbon content of TiO_2/C composite is calculated to 10%, which is consistent with the results based on TGA curves obtained in air and N_2

atmosphere.

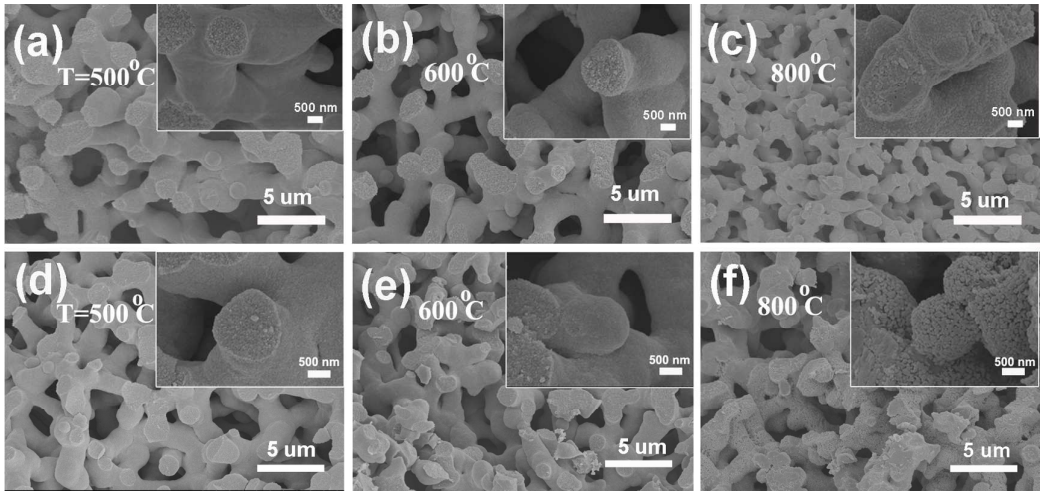

Fig. 5 SEM images of pure TiO_2 (a-c) and TiO_2/C composite (d-f) calcined at different temperatures. Insets are the corresponding high magnification images.

Fig. 5 shows SEM images of pure TiO_2 and TiO_2/C composite calcined at different temperatures. It can be seen that all of them demonstrate a interconnected macroporous structure, which are formed by phase separation induced by PVP at the same instant as the sol-gel transition.[54,58-60] As shown in Fig. 5, the typical size of cocontiuous macropores is in the range of 1-3 μm in diameter. The high-magnification SEM images (insets) reveal that these skeleton surface consists of many fine nanocrystals. With the increase of temperature, the porosity decreases due to the increase of average grain size, resulting in more compact skeletons. Larger nanoparticles and some aggregations occur at the high temperature of 800 °C (inset of Fig. 5c), which could be attributed to the effect of sintering. Compared to pure TiO_2, the surface of TiO_2/C composite becomes rough and some nanoparticles emerge with the increasing of calcination temperature. Some isolated particles coating appear on the surface of skeletion after calcination at 800 °C

(inset of Fig. 5f) due to the formation of carbon originated from the pyrolysis of PVP.

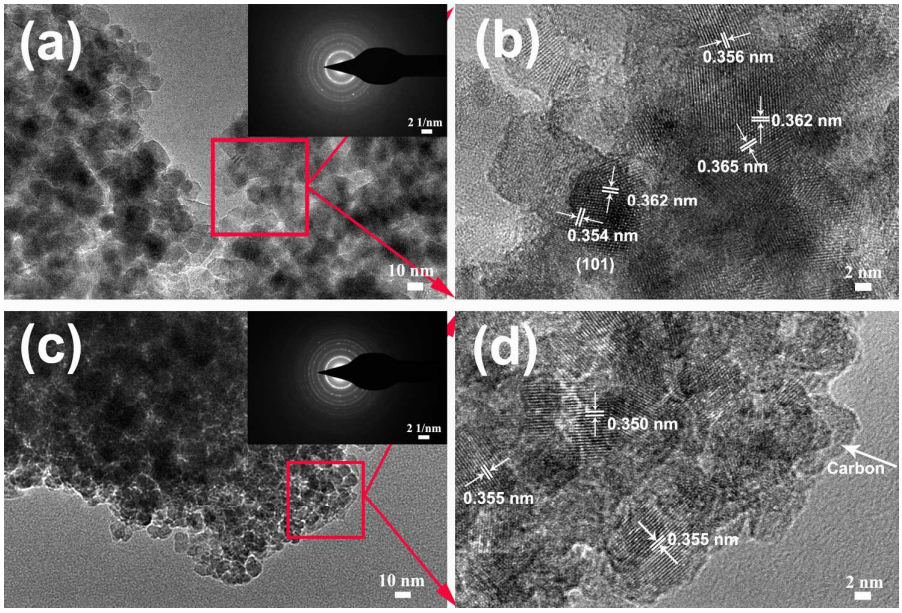

Fig. 6 (a and b) TEM and HRTEM images of pure TiO_2. (c and d) TEM and HRTEM images of TiO_2/C composite. The insets are corresponding SAED images and both the samples calcined at 500 °C.

The detail microstructure of pure TiO_2 and TiO_2/C composite was further investigated by TEM and HRTEM analysis. As revealed in Fig. 6, both of samples display the morphology characteristic of porous structure assembled with fine nanocrystals with the size of 10-30 nm (Fig. 6a and c). The result is consistent well with SEM images. The polycrystalline structure of both samples can be confirmed by the selected area electronic diffraction pattern (inset in Fig. 6a and c), moreover, the distinct lattice stripes in the HRTEM images (Fig. 6b and d) reveal the pure TiO_2 and TiO_2/C composite are well crystallized, and the lattice interplanar spacings of approximately 0.36 nm correspond to the (101) plane of tetragonal TiO_2, in good agreement with the results of XRD (Fig. 2). Furthermore, compared

to pure TiO_2, some grey regions marked by white arrow in Fig. 6d could be detected for TiO_2/C composite, which could be attributed to the carbon derived from PVP.

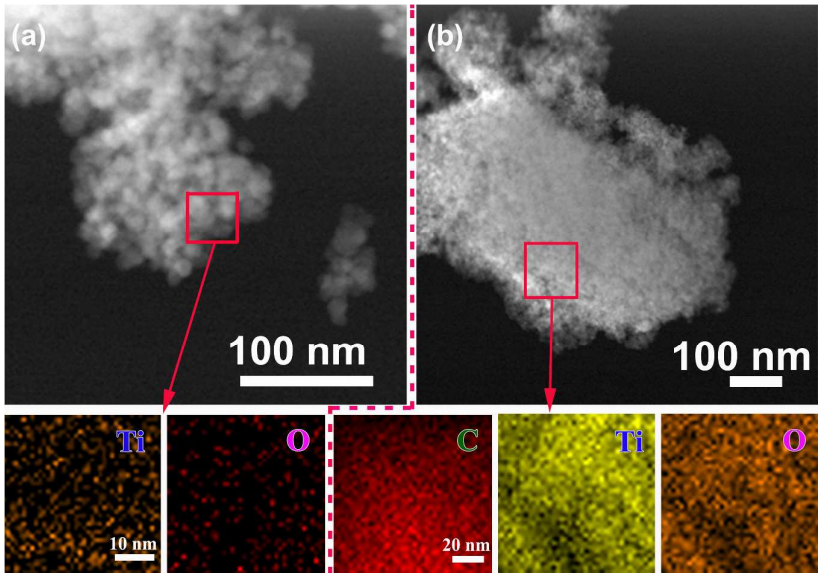

Fig. 7 STEM image and EDX mapping images of pure TiO_2 (a) and TiO_2/C composite (b), both the samples calcined at 500 °C.

Scanning transmission electron microscope (STEM) and area-scan elemental mapping tests were carried out to verify the composition of pure TiO_2 and TiO_2/C composite. As seen in Fig. 7a, pure TiO_2 exhibits rough surface, which is similar to the SEM results. The energy-dispersive spectroscopy (EDS) mappings (Fig. 7a) corresponding to the area outlined by the red square demonstrate titanium and oxygen elements are dispersed homogeneously, implying the uniform chemical composition of pure TiO_2 without any other elements. Meanwhile, the detailed microstructure and elements mappings of TiO_2/C composite are investigated. As shown in Fig. 7b, the uniform element distribution of C, Ti and O can be detected, indicating the *in situ* formed carbon is tightly contacted with TiO_2 particles, which

authentically confirms the above mentioned results of Raman spectra and TEM images.

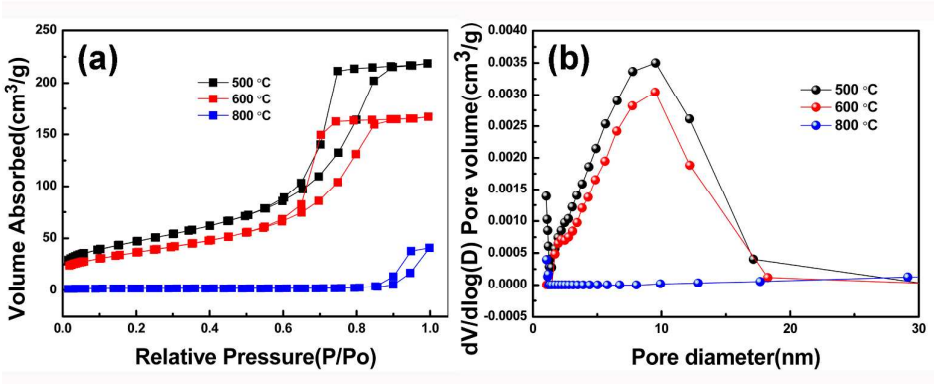

Fig. 8 Nitrogen adsorption-desorption isotherms (a) and pore size distributions curves (b) of TiO_2/C composite measured at 77 K.

The mesoporous characteristic was investigated by nitrogen isothermal absorption-desorption measurements. Fig. 8a shows the isotherm curve of TiO_2/C composite calcined at different temperature, the obtained specific parameters of TiO_2/C composite samples are shown in Table 1. Samples calcined at 500 and 600 °C present a typical type IV with H1 hysteresis loops at relative pressure of 0.65-0.85 according to IUPAC classification, representing the mesoporous structure.[28,61,62] The BET specific surface area of samples calcined at 500, 600 and 800 °C are identified to be 170 ,132 and 7 $m^2 g^{-1}$, respectively. The surface area and pore volume decrease as temperature increases, which could be ascribed to the effect of sintering and the growth of grains. Additionally, the pore size distribution curves (Fig. 8b) indicate most pores are around 10 nm for the samples calcined at 500 and 600 °C. Compared with pure TiO_2 (Fig. S3 and Table S2), TiO_2/C composite presents a larger specific surface area with a smaller average pore size due to the smaller grain size. The results are consistent with XRD patterns shown

in Fig. 2.

Table 1 Pore characteristics of TiO_2/C composite calcined at different temperature.

Sample	Calcination Temperature (°C)	Time (h)	S_{BET} (m^2/g)	V_p (cm^3/g)
TiO_2/C composite	500	4	170	0.338
TiO_2/C composite	600	4	132	0.258
TiO_2/C composite	800	4	7	0.063

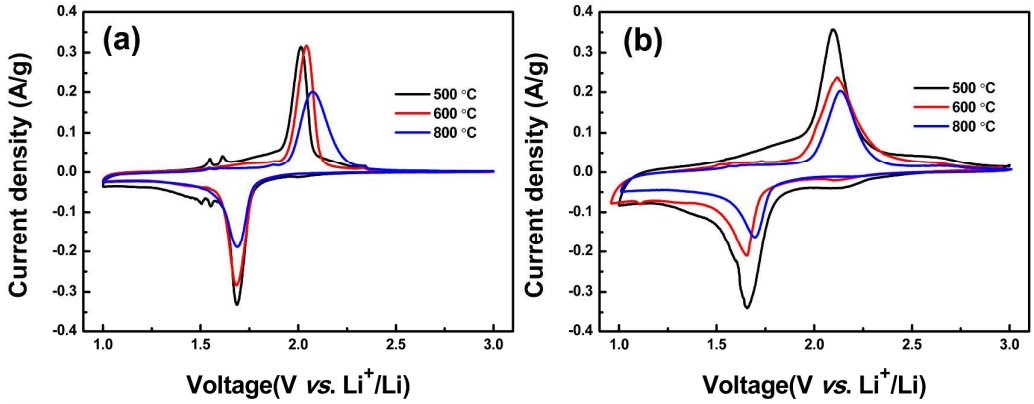

Fig. 9 The CV curves (2nd cycle) of pure TiO_2 (a) and TiO_2/C composite (b) electrodes at a scan rate of 0.1 mV s^{-1} in the potential window of 1.0-3.0 V.

Cyclic voltammetry is a complementary technique to galvanostatic cycling and helps in understanding the nature and potentials at which the discharge-charge reactions take place in the electrode material. Fig. 9 shows the CV curves of pure TiO_2 and TiO_2/C composite electrodes at a scanning rate of 0.1 mV s^{-1} from 1 to 3 V. It can be seen that all the samples display typical electrochemical characteristics of anatase TiO_2 with a sharp pair of redox peaks at about 1.68 and 2.1 V, corresponding to the two-phase processes of lithium insertion/extraction in the anatase phase ($xLi^+ + TiO_2 + xe^- \leftrightarrow Li_xTiO_2$).[63,64] The intensity of peaks reflect the electrochemical performance of electrode materials, as shown in Fig.9 a and b,

the intensity of peaks decreases with the increase of temperature, agrees with the result of galvanostatic charge-discharge tests (shown below). Moreover, there are two small redox peaks between 1.5 and 1.6 V are observed for pure TiO_2 calcined at 500 °C, which could be attributed to the trace amount of TiO_2-B, a low temperature phase of TiO_2, which could be irreversible transformed to anatase with the increase of temperature. [9,19,64] Compared to pure TiO_2 samples, the background of the redox peaks for TiO_2/C composites (Fig. 9b) are much more wider than that of pure ones (Fig. 9a), which can be assigned to the pseudocapacitive, faradaic-limited process derived from the carbon.[65]

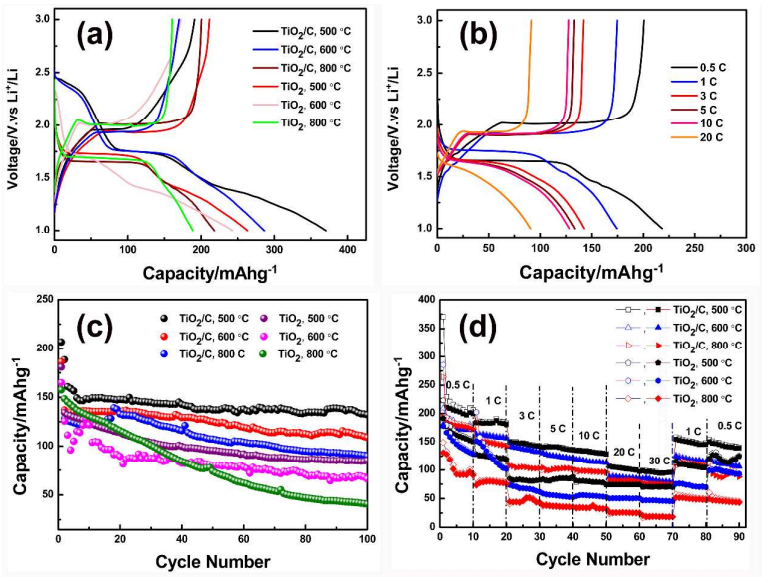

Fig. 10 Electrochemical properties of pure TiO_2 and TiO_2/C composite:(a) Initial charge and discharge curves at 0.5 C (1C=168 mAh g^{-1}). (b) Charge and discharge profiles (2nd cycle) of TiO_2/C composite calcined at 500 °C at different rates. (c) Cycling performance at 1 C. (d) Rate performance at various rates. All the tests are conducted with a voltage window of 1.0-3.0 V.

The electrochemical properties of pure TiO_2 and TiO_2/C composite calcined at different temperatures for Li-ion battery applications were evaluated by galvanostatic charge-discharge tests, and the specific capacities are calculated based on the weight of the whole active material in this work. Fig. 10a displays the

first galvanostatic charge-discharge profiles at 0.5 C. Agree well with the result of CV curves, a discharge voltage plateau at around 1.70±0.5 V and a charge voltage plateau at around 1.97±0.5 V are detected in all samples, the detail information of voltage plateau is shown in Table S3.[40,41] Large irreversible capacities were observed in all samples, which may be ascribed to the formation of Li_2O by H_2O/OH groups on the TiO_2 surfaces for the samples calcined at 500 and 600 °C, because these samples possess relatively high specific surface areas.[28,37] Additionally, the irreversible capacity of the sample calcined at 800 °C, composed of anatase and rutile, is due to the irreversible phase transformation from rutile to $LiTiO_2$.[66] TiO_2/C composite presents higher capacities than pure TiO_2, which could be attributed to the higher electronic conductivity contributed from the *in situ* produced carbon. The first discharge capacities of pure TiO_2 samples calcined at 500, 600, and 800 °C are 263, 243, and 189 mAh g^{-1}, respectively, corresponding to insertion of 0.78, 0.72 and 0.56 mole of Li per mol of TiO_2. Compared with pure TiO_2, TiO_2/C composite delivers a higher initial discharge capacity with 371 (1.1 mole of Li), 286 (0.85 mole of Li), and 217 mAh g^{-1} (0.64 mole of Li) calcined at 500, 600, and 800 °C, respectively. The high discharge capacity of TiO_2/C composite is contributed to the synthetic effect of insertion of Li for TiO_2 and surface lithium storage resulting from carbon.[49,65]

Fig. 10b presents the discharge-charge (2nd cycle) curves of the TiO_2/C composite electrode calcined at 500 °C at various rates (0.5-20 C). The capacity and the potential plateau (Table S4) both decrease with increasing current density

due to the polarization of electrode materials. The discharge capacities at various rates of 0.5, 1, 3, 5, 10 and 20 C are 217, 173, 142, 133, 127 and 89 mAh g^{-1}, respectively. A plateau at about 1.7 V, corresponding to a biphasic transition from the tetragonal TiO_2 to the orthorhombic $Li_{0.5}TiO_2$, and disappears completely at the high rate of 20 C, which could be attributed to the hierarchical porous anatase TiO_2 is capacitive lithium storage dominant at high rates instead of the solid-state diffusion reaction.[26,28,67] The capacitive effect may make cycling performance more stable (as shown in Fig. 10d) due to reversible surface lithium storage, which avoids the lattice expansion.

Fig. 10c compares the cyclic stability between pure TiO_2 and TiO_2/C composite electrodes in the voltage range of 1-3 V at 1 C. It can be seen that the discharge capacities of all samples decrease with increasing temperature. The discharge capacities of pure TiO_2 electrode calcined at 500, 600 and 800 °C decay quickly upon cycles, which could only remain 85, 66 and 41 mAh g^{-1} after 100 cycles, respectively. Compared to pure TiO_2 electrode, TiO_2/C composite present better cycling performance, the discharge cpacities remain relatively stable along with cycles. Discharge capacities of TiO_2/C composite calcined at 500, 600 and 800 °C could keep 132, 110 and 93 mAh g^{-1} after 100 cycles, respectively. The distinct difference between TiO_2/C composite and pure TiO_2 is ascribed to the higher electronic conductivity contributed from the *in situ* produced carbon and the larger contact area of the electrode and electrolyte.

To demonstrate the rate performance, the pure TiO_2 and TiO_2/C composite

samples were progressively charged and discharged from 0.5 to 30 C for 10 cycles at each rate, and then again at 1 and 0.5 C for 10 cycles, as shown in Fig. 10d. The result is consitent with Fig. 10c, TiO_2/C composites exhibit superior rate capability than pure TiO_2. It can be seen that the discharge and charge capacities of TiO_2/C composite samples remain stable and decrease regularly when the rate is increased from 0.5 to 30 C. While the capacities of pure TiO_2 fade rapidly even at low rates of 0.5 and 1C, which could be attributed to slow electron transport resulting from poor electrical conductivity. Meanwhile, compared with the sample calcined at 500 °C, a substantial decrease in capacity was observed when the calcination temperature was raised to 600 and 800 °C respectively, which is ascribed to the decrease of BET surface area resulting from the increment in crystal size and the disappearing of small mesopores. Moreover, when the current density is restored to 1 and 0.5 C again, specific capacities can be recovered to a large extent due to the unique hierarchically porous structure, and keep stable during continuous discharge/charge cycles. The performance of hierarchically porous TiO_2 based composite reported here is compared favourably to those of TiO_2 based electrodes reported in previous works.[27,38,39,57,68,69]

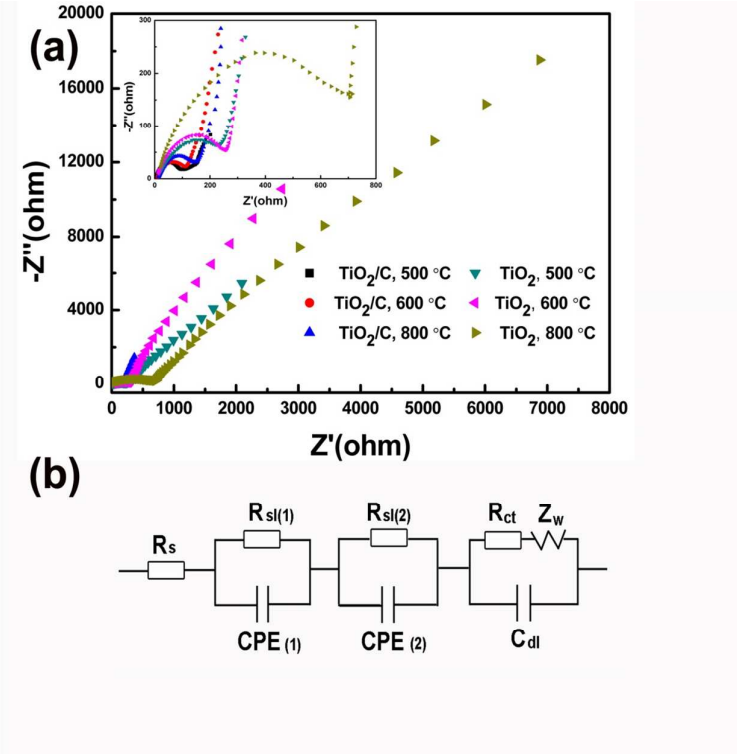

Fig. 11 (a) Electrochemical impedance spectra (EIS) of pure TiO_2 and TiO_2/C composite after three cycles (the inset shows the enlarged Nyquist plots). (b) the equivalent circuit used for fitting the the EIS curves.

Electrochemical impedance spectroscopy (EIS) of pure TiO_2 and TiO_2/C composite after three cycles was investigated, the corresponding Nyquist plots and enlarged Nyquist plots (inset) are shown in Fig. 11a. All the Nyquist plots exhibit a semicircle in the high frequency region and a sloping straight line in the low frequency region. The high frequency semicircle is ascribed to the charge-transfer impedance at the electrolyte/electrode interface, and the sloping straight line in low frequency region corresponds to the lithium ion diffusion process in the electrodes.[70,71] Fig. 11b presents the equivalent circuit, R_s is the solution resistance, R_{sl} (i) and CPE (i) (i = 1, 2) represent the migration of hydrogen ions and the capacity of the layer, respectively[72]. R_{ct} and C_{dl} denote the charge-transfer resistance and a double-layer capacitance, respectively.[73] Z_W is the Warburg

impedance. It can be seen from the inset of Fig. 11a that all the samples show a similar shape in the low frequency region, while in the case of the high frequency region, the size of semicircle increases with the increase of temperature. Meanwhile, compared with pure TiO_2, TiO_2/C composite exhibits smaller semicircle. Therefore, the TiO_2/C composite calcined at 500 °C shows the smallest semicircle, and pure TiO_2 calcined at 800 °C displays the biggest semicircle. The EIS measurement results indicate that TiO_2/C composite possesses lower charge-transfer resistance and contact resistance than those of pure TiO_2, resulting in better electrochemical performance due to higher reactivity and reaction kinetics. It could be attributed to the improved electronic conductivity of the TiO_2/C composite derived from carbon and large specific surface area resulting from small crystal particles.[74,75]

The outstanding electrochemical performance of TiO_2/C composite can be ascribed to its unique hierarchically porous nanoarchitecture, as shown in Fig. 12. Firstly, the interconnected porosity provides rich open channels, which improves the wettability of the electrolyte and offer more favorable paths for electrolyte penetration. In addition, the porous structure may also alleviate the strain induced by the volume change during the Li^+ insertion/extraction processes. Secondly, the assembled TiO_2 nanocrystals (10-30 nm) reduce the Li^+ diffusion distance and provide large BET specific surface area, ensuring better contact between the electrode material and the electrolyte. Additionally, the carbon derived from the pyrolysis of PVP effectively enhances the electrical conductivity of TiO_2 for the

rapid electrochemical reactions, therefore leading to superior rate capability. Consequently, the synergistic effects of the hierarchically porous structure and the incorporation of conductive carbon materials result in excellent cycling stability and rate capability.

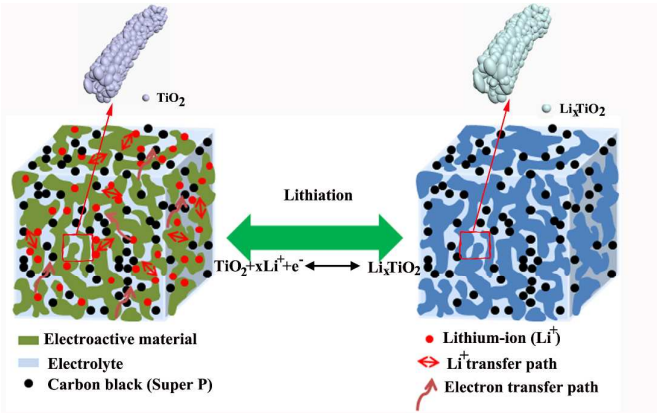

Fig. 12 schematic description of the paths for the electron and lithium-ion transport in the hierarchically porous TiO_2 based composites electrode.

Conclusions

In summary, unique porous TiO_2 and TiO_2/C composite were successfully prepared by a facile sol-gel process followed by post-calcination treatment. These TiO_2 based composites display a characteristic of hierarchically porous structure constructed by interconnecting nanocrystals, shortening lithium ion transmission pathway for high rate performance, and then the porous structure provides large space for alleviating volume change of TiO_2 during cycling. Moreover, the *in situ* formed carbon derived from PVP guarantees a rapid electrons transport during repeated charge/discharge processes. Thus, the resultant TiO_2/C composite exhibits excellent cycling stability and superior rate capability as anode materials for LIBs. We believe that this facile synthesis method can be extended to other

composites (such as $Li_4Ti_5O_{12}$, TiO_x, etc.) for a variety of energy conversion and storage applications.

Acknowledgements

This work was supported by the National Natural Science Foundation of China (51372225), and the Natural Science Foundation of Zhejiang Province, China (LY13B010001).

Notes and references

1 N. Roy, Y. Sohn and D. Pradhan, *Acs Nano* 2013, **7**, 2532.

2 Z. Y. Liu, D. D. L. Sun, P. Guo and J. O. Leckie, *Nano Lett*. 2007, **7**, 1081.

3 G. Wang, Q. Wang, W. Lu and J. H. Li, *J. Phys. Chem. B* 2006, **110**, 22029.

4 J. H. Huang, P. Y. Hung, S. F. Hu and R. S. Liu, *J. Mater. Chem*. 2010, **20**, 6505.

5 K. Pan, Y. Z. Dong, C. G. Tian, W. Zhou, G. H. Tian, B. F. Zhao and H. G. Fu, *Electrochim. Acta* 2009, **54**, 7350.

6 M. Stefik, F. J. Heiligtag, M. Niederberger and M. Gratzel, *Acs Nano* 2013, **7**, 8981.

7 D. Deng, M. G. Kim, J. Y. Lee and J. Cho, *Energ. Environ. Sci*. 2009, **2**, 818.

8 M. Wagemaker, A. P. M. Kentgens and F. M. Mulder, *Nature* 2002, **418**, 397.

9 H. Huang, Z. Y. Yu, W. J. Zhu, Y. P. Gan, Y. Xia, X. Y. Tao and W. K. Zhang, *J. Phys. Chem. Solids* 2014, **75**, 619.

10 H. Huang, J. W. Fang, Y. Xia, X. Y. Tao, Y. P. Gan, J. Du, W. J. Zhu and W. K. Zhang, *J. Mater. Chem. A* 2013, **1**, 2495.

11 Z. H. Bi, M. P. Paranthaman, P. A. Menchhofer, R. R. Dehoff, C. A. Bridges, M. F. Chi, B. K. Guo, X. G. Sun and S. Dai, *J. Power Sources* 2013, **222**, 461.

12 X. Chen and S. S. Mao, *Chem. Rev*. 2007, **107**, 2891.

13 J. S. Chen, D. Y. Luan, C. M. Li, F. Y. C. Boey, S. Z. Qiao and X. W. Lou, *Chem. Commun*. 2010, **46**, 8252.

14 J. W. Zhang, X. X. Yan, J. W. Zhang, W. Cai, Z. S. Wu and Z. J. Zhang, *J. Power Sources* 2012, **198**, 223.

15 S. T. Myung, N. Takahashi, S. Komaba, C. S. Yoon, Y. K. Sun, K. Amine and H. Yashiro, *Adv. Funct. Mater.* 2011, **21**, 3231.

16 Z. X. Yang, G. D. Du, Q. Meng, Z. P. Guo, X. B. Yu, Z. X. Chen, T. L. Guo and R. Zeng, *J. Mater. Chem.* 2012, **22**, 5848.

17 I. Moriguchi, R. Hidaka, H. Yamada, T. Kudo, H. Murakami and N. Nakashima, *Adv. Mater*. 2006, **18**, 69.

18 X. Su, Q. L. Wu, X. Zhan, J. Wu, S. Y. Wei and Z. H. Guo, *J. Mater. Sci.* 2012, **47**, 2519.

19 S. H. Liu, H. P. Jia, L. Han, J. L. Wang, P. F. Gao, D. D. Xu, J. Yang and S. N. Che, *Adv. Mater*. 2012, **24**, 3201.

20 Y. G. Guo, Y. S. Hu, W. Sigle and J. Maier, *Adv. Mater*. 2007, **19**, 2087.

21 J. Wang, Y. K. Zhou, Y. Y. Hu, R. O'Hayre and Z. P. Shao, *J. Phys. Chem. C* 2011, **115**, 2529.

22 J. F. Ye, W. Liu, J. G. Cai, S. A. Chen, X. W. Zhao, H. H. Zhou and L. M. Qi, *J. Am. Chem. Soc*. 2011, **133**, 933.

23 A. I. Hochbaum and P. D. Yang, *Chem. Rev*. 2010, **110**, 527.

24 H. J. Zhou, L. Liu, X. C. Wang, F. X. Liang, S. J. Bao, D. M. Lv, Y. K. Tang and D. Z. Jia, *J. Mater. Chem. A* 2013, **1**, 8525.

25 V. Gentili, S. Brutti, L. J. Hardwick, A. R. Armstrong, S. Panero and P. G. Bruce, *Chem. Mater*.

2012, **24**, 4468.

26 B. T. Zhao, S. M. Jiang, C. Su, R. Cai, R. Ran, M. O. Tade and Z. P. Shao, *J. Mater. Chem. A* 2013, **1**, 12310.

27 H. E. Wang, H. Cheng, C. P. Liu, X. Chen, Q. L. Jiang, Z. G. Lu, Y. Y. Li, C. Y. Chung, W. Y. Zhang, J. A. Zapien, L. Martinu and I. Bello, *J. Power Sources* 2011, **196**, 6394.

28 G. Hasegawa, T. Sato, K. Kanamori, K. Nakanishi and T. Abe, *New J. Chem*. 2014, **38**, 1380.

29 H. B. Wu, J. S. Chen, H. H. Hng and X. W. Lou, *Nanoscale* 2012, **4**, 2526.

30 X. Xu, B. Tian, J. Kong, S. Zhang, B. Liu and D. Zhao, *Adv. Mater*. 2003, **15**, 1932-1936.

31 I. Moriguchi, R. Hidaka, H. Yamada, T. Kudo, H. Murakami and N. Nakashima, Adv. Mater. 2006, **18**, 69-73.

32 W. Wang, M. Tian, A. Abdulagatov, S. M. George, Y. C. Lee and R. G. Yang, *Nano Lett*. 2012, **12**, 655.

33 Y. S. Luo, J. S. Luo, J. Jiang, W. W. Zhou, H. P. Yang, X. Y. Qi, H. Zhang, H. J. Fan, D. Y. W. Yu, C. M. Li and T. Yu, *Energ. Environ. Sci*. 2012, **5**, 6559.

34 K. S. Park, J. G. Kang, Y. J. Choi, S. Lee, D. W. Kim and J. G. Park, *Energ. Environ. Sci*. 2011, **4**, 1796.

35 Z. X. Yang, G. D. Du, Z. P. Guo, X. B. Yu, Z. X. Chen, T. L. Guo and R. Zeng, *Nanoscale* 2011, **3**, 4440.

36 Y. Qiao, X. L. Hu, Y. Liu, C. J. Chen, H. H. Xu, D. F. Hou, P. Hu and Y. H. Huang, *J. Mater. Chem. A* 2013, **1**, 10375.

37 W. S. Wang, Q. N. Sa, J. H. Chen, Y. Wang, H. J. Jung and Y. D. Yin, *Acs Appl. Mater. Inter*. 2013, **5**, 6478.

38 Z. X. Yang, Q. Meng, Z. P. Guo, X. B. Yu, T. L. Guo and R. Zeng, *J. Mater. Chemi. A* 2013, **1**, 10395.

39 L. C. Liu, Q. Fan, C. Z. Sun, X. R. Gu, H. Li, F. Gao, Y. F. Chen and L. Dong, *J. Power Sources* 2013, **221**, 141.

40 S. B. Yang, X. L. Feng and K. Mullen, *Adv. Mater*. 2011, **23**, 3575.

41 X. Xin, X. F. Zhou, J. H. Wu, X. Y. Yao and Z. P. Liu, *Acs Nano* 2012, **6**, 11035.

42 F. Sordello, G. Zeb, K. W. Hu, P. Calza, C. Minero, T. Szkopek and M. Cerruti, *Nanoscale* 2014, **6**, 6710.

43 Y. Luo, J. Luo, W. Zhou, X. Qi, H. Zhang, Y. Denis, C. M. Li, H. J. Fan and T. Yu, *J. Mater. Chem. A* 2013, **1**, 273.

44 C. M. Greenlief, J. M. White, C. S. Ko and R. J. Gorte, *J. Phys. Chem-Us*. 1985, **89**, 5025.

45 D. Song, J. Hrbek and R. Osgood, *Nano Lett*. 2005, **5**, 1327.

46 J. Y. Ruzick, F. Abu Bakar, L. Thomsen, B. C. Cowie, C. McNicoll, T. Kemmitt, H. E. A. Brand, B. Ingham, G. G. Andersson and V. B. Golovko, *Rsc Adv*. 2014, **4**, 20649.

47 A. D. C. Permana, A. Nugroho, K. Y. Chung, W. Chang and J. Kim, *Chem. Eng. J*. 2014, **241**, 216.

48 H. Yang, W. Zhu, S. Sun and X. Guo, *Rsc Adv*. 2014, **4**, 32934.

49 K. Hemalatha, A. S. Prakash, K. Guruprakash and M. Jayakumar, *J. Mater. Chem. A* 2014, **2**, 1757.

50 C. Lu, Y. Sun, J. Liu, X. Wang, S. L. Liu and W. Feng, *J. Appl. Polym. Sci*. 2015, **132**,41583.

51 X. B. Wang, Y. Y. Wang, L. Yang, K. Wang, X. D. Lou and B. B. Cai, *J. Power Sources* 2014, **262**, 72.

52 R. Nakamura and Y. Nakato, *J. Am. Chem. Soc*. 2004, **126**, 1290.

53 K. Nakanishi and K. Kanamori, *J. Mater. Chem*. 2005, **15**, 3776.

54 K. Nakanishi, *J. Porous. Mat*. 1997, **4**, 67.

55 G. Hasegawa, K. Kanamori, K. Nakanishi and T. Hanada, *J. Sol-Gel. Sci. Techn*. 2010, 53, 59.

56 H. C. Choi, Y. M. Jung and S. B. Kim, *Vib. Spectrosc*. 2005, **37**, 33.

57 P. Y. Chang, C. H. Huang and R. A. Doong, *Carbon* 2012, **50**, 4259.

58 W. Y. Li, X. Z. Guo, Y. Zhu, Y. Hui, K. Kanamori and K. Nakanishi, *J. Sol-Gel. Sci. Techn*. 2013, **67**, 639.

59 Y. Tokudome, N. Tarutani, K. Nakanishi and M. Takahashi, *J. Mater. Chem. A*, 2013, **1**, 7702.

60 K. Nakanishi and N. Tanaka, *Accounts Chem. Res*. 2007, **40**, 863.

61 H. Huang, W. Zhu, X. Tao, Y. Xia, Z. Yu, J. Fang, Y. Gan and W. Zhang, *Acs Appl. Mater. Inter*. 2012, **4**, 5974.

62 W. Zhu, H. Huang, Y. Gan, X. Tao, Y. Xia and W. Zhang, *Electrochim. Acta* 2014, **138**, 376.

63 C. T. Cherian, M. V. Reddy, T. Magdaleno, C. H. Sow, K. V. Ramanujachary, G. V. S. Rao and B. V. R. Chowdari, *Crystengcomm*. 2012, **14**, 978.

64 P. C. Chen, M. C. Tsai, H. C. Chen, I. N. Lin, H. S. Sheu, Y. S. Lin, J. G. Duh, H. T. Chiu and C. Y. Lee, *J. Mater. Chem*. 2012, **22**, 5349.

65 Y. Gan, L. Zhu, H. Qin, Y. Xia, H. Xiao, L. Xu, L. Ruan, C. Liang, X. Tao and H. Huang, *Solid State Ionics* 2015, **269**, 44.

66 E. Baudrin, S. Cassaignon, M. Koelsch, J.-P. Jolivet, L. Dupont and J.-M. Tarascon, *Electrochem. Commun*. 2007, **9**, 337.

67 J. Wang, Y. K. Zhou, Y. Y. Hu, R. O'Hayre and Z. P. Shao, *J. Mater. Sci*. 2013, **48**, 2733.

68 Y. C. Qiu, K. Y. Yan, S. H. Yang, L. M. Jin, H. Deng and W. S. Li, *Acs Nano* 2010, **4**, 6515.

69 D. H. Wang, D. W. Choi, J. Li, Z. G. Yang, Z. M. Nie, R. Kou, D. H. Hu, C. M. Wang, L. V. Saraf, J.

G. Zhang, I. A. Aksay and J. Liu, *Acs Nano* 2009, **3**, 907.

70 R. Mo, Z. Lei, K. Sun and D. Rooney, *Adv. Mater.* 2014, **26**, 2084.

71 C. L. Zhang, Q. Y. Zhang, S. F. Kang and X. Li, *J. Mater. Chem. A* 2014, **2**, 2801.

72 G. F. Cai, J. P. Tu, D. Zhou, J. H. Zhang, Q. Q. Xiong, X. Y. Zhao, X. L. Wang and C. D. Guts, *J. Phys. Chem. C* 2013, **117**, 15967.

73 Y. Xia, Z. Xiao, X. Dou, H. Huang, X. H. Lu, R. J. Yan, Y. P. Gan, W. J. Zhu, J. P. Tu, W. K. Zhang and X. Y. Tao, *Acs Nano* 2013, **7**, 7083.

74 J. Jin, S. Z. Huang, J. Liu, Y. Li, D. S. Chen, H. E. Wang, Y. Yu, L. H. Chen and B. L. Su, *J. Mater. Chem. A* 2014, **2**, 9699.

75 L. Tan, L. Pan, C. Y. Cao, B. F. Wang and L. Li, *J. Power Sources* 2014, **253**, 193.

Sol-gel synthesis of nanocrystals-constructed hierarchically porous TiO_2 based composites for lithium ion batteries

Wenjun Zhu,[a] Hui Yang,[a] Kazuki Nakanishi,[b] Kazuyoshi Kanamori,[b] Xingzhong Guo*[a]

[a]School of Materials Science and Engineering, Zhejiang University, 38 Zheda Road, Xihu District, Hangzhou 310027, China

[b]Department of Chemistry, Graduate School of Science, Kyoto University, Kitashirakawa, Sakyo-ku, Kyoto 606-8502, Japan.

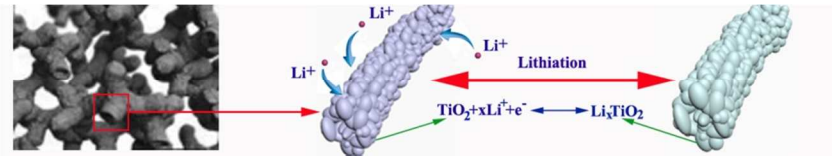

A facile synthesis strategy of hierarchically porous TiO_2 based composites has been proposed. The as-prepared TiO_2 based composites possess an interesting hierarchically porous structure constructed by cocontinuous macropores and mesoporous skeletons consisting of interconnected nanocrystals and *in-situ* distributed carbon. As anode materials for lithium-ion batteries (LIBs), which exhibit excellent cycling stability and superior rate capability.